

Decadal Variability of Eddy Kinetic Energy in the South Pacific Subtropical Countercurrent in an Ocean General Circulation Model

JAN K. RIECK, CLAUS W. BÖNING, AND RICHARD J. GREATBATCH

GEOMAR Helmholtz Centre for Ocean Research Kiel, Kiel, Germany

(Manuscript received 31 August 2017, in final form 24 January 2018)

ABSTRACT


The eddy kinetic energy (EKE) associated with the Subtropical Countercurrent (STCC) in the western subtropical South Pacific is known to exhibit substantial seasonal and decadal variability. Using an eddy-permitting ocean general circulation model, which is able to reproduce the observed, salient features of the seasonal cycles of shear, stratification, baroclinic production, and the associated EKE, the authors investigate the decadal changes of EKE. The authors show that the STCC region exhibits, uniquely among the subtropical gyres of the world's oceans, significant, atmospherically forced, decadal EKE variability. The decadal variations are driven by changing vertical shear between the STCC in the upper 300 m and the South Equatorial Current below, predominantly caused by variations in STCC strength associated with a changing meridional density gradient. In the 1970s, an increased meridional density gradient results in EKE twice as large as in later decades in the model. Utilizing sensitivity experiments, decadal variations in the wind field are shown to be the essential driver. Local wind stress curl anomalies associated with the interdecadal Pacific oscillation (IPO) lead to upwelling and downwelling of the thermocline, inducing strengthening or weakening of the STCC and the associated EKE. Additionally, remote wind stress curl anomalies in the eastern subtropical South Pacific, which are not related to the IPO, generate density anomalies that propagate westward as Rossby waves and can account for up to 30%–40% of the density anomalies in the investigated region.

1. Introduction

During the last decade, it has become evident that a large fraction of variability in the global ocean is intrinsic in the sense that no interannual-to-decadal atmospheric variability is needed to drive oceanic variability on these time scales. Studies utilizing ocean general circulation models (OGCMs) have shown this intrinsic variability to manifest itself in sea surface height (SSH) variance (Combes and Di Lorenzo 2007; Penduff et al. 2011; Sérazin et al. 2015) as well as eddy kinetic energy (Wilson et al. 2015). Even properties not directly related to the mesoscale, such as the Atlantic meridional overturning circulation (AMOC) (Grégorio et al. 2015), ocean heat content (Sérazin et al. 2017), and sea level trends (Sérazin et al. 2016), exhibit intrinsic variability.

Nevertheless, there are regions with lower intrinsic variability on interannual-to-decadal time scales. These regions are mainly, but not exclusively, located in the tropical oceans, where the ocean dynamics are relatively linear and largely depend on air–sea interactions (Penduff et al. 2011; Sérazin et al. 2015). Apart from these areas, the interior subtropical South Pacific (SP) exhibits relatively weak intrinsic variability of SSH at $\sim 30^{\circ}\text{S}$, compared to that found in the other subtropical oceans (Sérazin et al. 2015).

In the subtropical SP, the Subtropical Countercurrent (STCC; Travis and Qiu 2017), initially called the South Tropical Countercurrent (Merle et al. 1969; Morris et al. 1996), is located between 25° and 33°S on top of the large-scale gyre circulation. Contrary to the gyre circulation, which flows westward in the South Equatorial Current (SEC) at these latitudes, the STCC flows eastward, thereby creating a vertical shear of horizontal velocities. Similar current systems, associated with subtropical or similar fronts, can be found in the North Pacific (Kobashi and Kubokawa 2012) and Indian Oceans (Menezes et al. 2014). The vertical shear in these systems is generally baroclinically unstable

 Denotes content that is immediately available upon publication as open access.

Corresponding author: Jan K. Rieck, jriek@geomar.de

(e.g., Qiu 1999; Qiu and Chen 2004) and generates mesoscale variability.

Depending on the current systems, the mesoscale variability exhibits variability on different time scales. The North Pacific Subtropical Countercurrent, the STCC, and parts of the South Indian Countercurrent (SICC) all have been shown to generate more mesoscale turbulence in summer than in winter (Qiu 1999; Qiu and Chen 2004; Jia et al. 2011b). These seasonal variations are driven by an increased meridional density gradient across the associated fronts in summer, inducing a stronger, surface-intensified current, and thus enhanced shear with the underlying currents. The source of the increased meridional density gradient can be either dynamic or thermodynamic. In the South Pacific, Qiu and Chen (2004) argue for latitudinally dependent surface cooling to be the main factor in the STCC. However, Jia et al. (2011b) show Ekman and geostrophic flux convergence to be responsible in the SICC. The variability in countercurrent systems is not restricted to the seasonal time scales. The SICC has been shown to vary with a quasi-biennial period (Menezes et al. 2016) and interannually (Jia et al. 2011a) due to changes in the meridional density gradient driven by anomalous Ekman upwelling (Jia et al. 2011a), which they relate to changes in the wind field associated with the southern annular mode. Qiu and Chen (2010) argue that the interannual variability in the North Pacific Subtropical Countercurrent is generated by surface heat flux forcing related to the Pacific decadal oscillation.

More recently, Travis and Qiu (2017) investigated the decadal variations of instability in the STCC region. The decadal changes are caused by a combination of variations of vertical shear of velocities and stratification. Stronger (weaker) vertical shear and weaker (stronger) stratification both induce enhanced (decreased) instability. Travis and Qiu (2017) find the variability of vertical shear to be the dominant mechanism. However, they did not determine which factors ultimately drive the associated density changes observed in the STCC. Decadal variability in SP SSH has been shown to affect the large-scale gyre circulation (Roemmich et al. 2016), as well as local EKE levels associated with the Tasman Front (Sasaki et al. 2008). Sasaki et al. (2008) show that basin-scale wind stress curl variations related to decadal modulations in El Niño–Southern Oscillation (ENSO) drive the SSH and EKE changes. An influence on the STCC system and associated EKE can thus be expected.

In this study, the use of an OGCM enables us to extend our knowledge of the STCC and its variability because of a long study period of more than five decades and a deeper investigation of mechanisms. We show that the decadal variability of surface currents and EKE is

related to atmospheric forcing rather than internal variability in the STCC region (section 3a). Furthermore, we validate the mean state of the STCC and associated mesoscale variability from the OGCM in section 3b, and in section 3c, we show that the OGCM is able to reproduce the seasonal cycle of EKE. Then, in section 3d, we investigate the decadal variations, and in section 3e, we investigate the role of the atmospheric forcing in the context of decadal variability associated with the interdecadal Pacific oscillation (IPO).

2. Model, methods, and data

This study is based on an eddy-permitting global ocean circulation model using a $1/4^\circ$ configuration (ORCA025) based on the NEMO code (Madec et al. 1998) version 3.6, developed as part of the DRAKKAR collaboration. It is accompanied by an additional configuration (TROPAC01) with a refined grid in the South Pacific. As a base, TROPAC01 has a global $1/2^\circ$ horizontal grid (ORCA05) and shares the vertical levels with ORCA025. Between 49°S and 31°N in the Pacific, a grid with $1/10^\circ$ resolution is nested into the ORCA05 grid using adaptive grid refinement in Fortran (AGRIF; Debreu et al. 2008). TROPAC01 has been compared to observations in Czeschel et al. (2011) and van Sebille et al. (2014). For more information on TROPAC01, the reader is referred to Schwarzkopf (2016).

Hindcast experiments were performed with the two configurations from 1958 to 2009 and 1960–2007 for ORCA025 and TROPAC01, respectively. Comparing these hindcast experiments, it is shown that the ORCA025 configuration has about 60%–70% of the mesoscale variability of TROPAC01 in the subtropical South Pacific (see section 3d). Most importantly, ORCA025 is able to reproduce the relative amplitude of the decadal variability simulated in TROPAC01 (Figs. 1a,b and sections 3a and 3d). Thus, the several sensitivity experiments carried out as part of this study have been performed with the ORCA025 configuration.

The various ORCA025 configurations developed in recent years (Barnier et al. 2007, 2014) share the same global, orthogonal, curvilinear, tripolar Arakawa C-type grid with a nominal resolution of $1/4^\circ$ in longitude. ORCA025 configurations have been widely used in studies investigating ocean variability mechanisms in different areas (e.g., Lübbecke et al. 2008; Lorbacher et al. 2010; Rühls et al. 2015), as well as influences of large-scale atmospheric variability on the ocean (e.g., Feng et al. 2011; Ummenhofer et al. 2013; Barrier et al. 2015) and intrinsic oceanic variability on different time scales (Penduff et al. 2010; Sérazin et al. 2015).

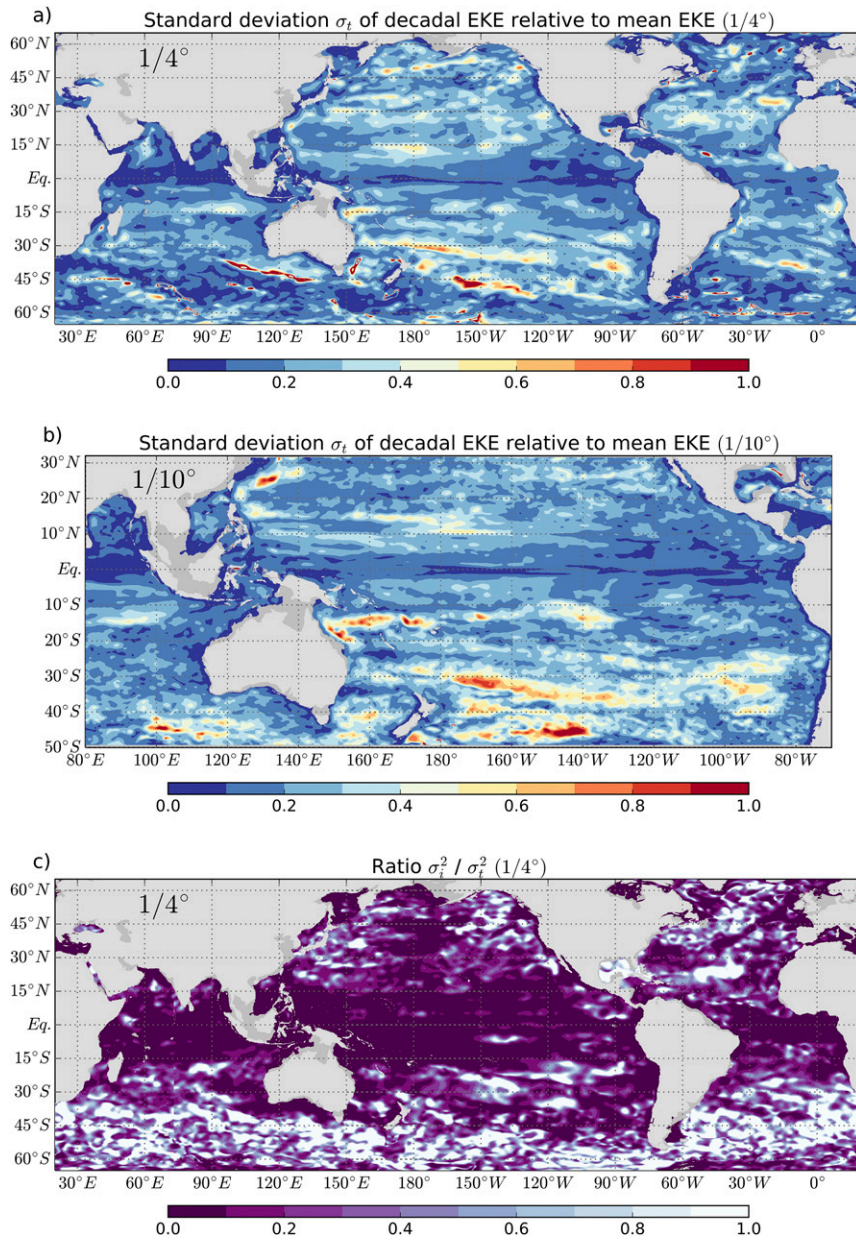


FIG. 1. (a) The standard deviation of decadal smoothed EKE from ORCA025 (REF; 1963–2006) at 93 m (a low-pass Lanczos filter with a 5-yr cutoff period is used at every grid point), divided by the mean EKE (REF; 1963–2006) at each grid point. A value of one indicates the amplitude of decadal EKE variations to be as large as the mean EKE, while a value close to zero depicts a grid point without significant EKE variability on decadal time scales. (b) As in (a), but for the $1/10^\circ$ resolution domain of TROPAC01. (c) The ratio of variance of decadal smoothed intrinsic EKE from CLIM (93-m depth, years 16–59) to variance of decadal smoothed total EKE from REF (93-m depth, 1963–2006) as described in section 3a. A ratio of one indicates that all variability is intrinsic, while values close to zero show grid points where most of the variability is deterministic.

The particular (Kiel) version of ORCA025 employed here uses 46 vertical levels with 6-m thickness at the surface, increasing toward ~ 250 m in the deep ocean and a partial-cell formulation at the bottom (cf. Barnier

et al. 2006). The atmospheric forcing for the simulations from 1958 to 2009 utilizes the bulk formulations and data products in the Co-ordinated Ocean–Ice Reference Experiments (CORE.v2; Griffies et al. 2009; Large and

Yeager 2009). The CORE.v2 products are available for the period 1948–2009; however, some forcing fields are climatological in the first decades of the forcing. Starting the simulations from 1958 thus constitutes a compromise between using a long study period to investigate decadal variability and discarding the decades with highest uncertainty from the forcing. All model simulations apply a very weak sea surface salinity restoring (SSSR) to climatology of $33.33 \text{ mm day}^{-1}$, which corresponds to a relaxation time scale of 1500 days over a 50-m surface layer.

The model is spun up from rest with temperature and salinity from climatology (PHC2.1 updated from Steele et al. 2001) and an initial sea ice field from 31 December 1992 from a previous ORCA025 simulation, as this sea ice state fits the initial temperature and salinity fields. The model spinup is forced for 30 years with the atmospheric forcing from 1980 to 2009. The ocean state at the end of this spinup period is then used as the initial condition for the hindcast simulations. Five experiments have been simulated in total: REF, CLIM, WIND, BUOY, and IPOsim (Table 1).

REF (1958–2009) is the reference simulation with no changes to the forcing described above, in order to represent a realistic estimate of the simulated period. The CLIM simulation (62 years) with a repeating normal year (NY; Large and Yeager 2009) forcing is used to study the relative importance of intrinsic and forced variability. WIND (1958–2009) applies an interannually varying wind stress forcing in combination with climatological NY buoyancy forcing (heat and freshwater fluxes). WIND is accompanied by BUOY, which utilizes an interannually varying buoyancy forcing in combination with an NY wind stress forcing. The latter two experiments are intended to determine whether decadal variations in the STCC can be related to wind or buoyancy forcing from the atmosphere. The fifth experiment, IPOsim (28 years), starts with 3 years of NY forcing. For the following 10 years, the annual mean wind field of the NY forcing is replaced by a mean wind field representative of a negative state of the IPO, while keeping the synoptic variability and seasonal cycle of the NY forcing. This negative IPO phase is followed by 10 years where the mean wind field represents a positive IPO. The experiment concludes with 5 more NY-forced years. The IPO phases are defined after the IPO tri-pole index (TPI) from Henley et al. (2015) to be the averaged wind field over 1970–75 and 1980–85 for the negative and positive phases, respectively. During the first and last years of the 10-yr negative (positive) IPO phase, the mean wind field is linearly interpolated from the climatological state to the negative (positive) IPO state and back toward climatology, respectively.

TABLE 1. Length and forcing of the five main experiments; see section 2 for more details. More information on the experiments can be found alongside the data (<http://data.geomar.de>).

Experiment	Length	Wind stress forcing	Buoyancy forcing
REF	1958–2009	Full	Full
CLIM	62 years	Normal year	Normal year
WIND	1958–2009	Full	Normal year
BUOY	1958–2009	Normal year	Full
IPOsim	28 years	IPO	Normal year

EKE is defined to be $EKE = 0.5(u'^2 + v'^2)$, where $(u', v') = (u - \bar{u}, v - \bar{v})$. Variables (u, v) represent the 5-day mean zonal and meridional velocities at 93-m depth, respectively, and (\bar{u}, \bar{v}) are the 1-yr mean horizontal velocities at 93-m depth. One-year mean velocities (\bar{u}, \bar{v}) are used as to avoid interannual variations of the mean currents to be considered in the calculation of EKE. For further details on the calculation of EKE, see Penduff et al. (2004) and Rieck et al. (2015). All investigations of near-surface circulation and EKE from the model output are performed at a depth of 93 m to exclude any ageostrophic circulation features, such as Ekman currents, that are present at the surface. To allow for the equilibration of EKE after the spinup, the first 2 years of all hindcast experiments are discarded from use in the analysis (so that the periods used from REF, CLIM, WIND, and BUOY are 1960–2009).

All model output and the derived quantities have been detrended prior to any averaging applied. When monthly time series are shown, the climatological seasonal cycle has been removed as well. Unless otherwise stated, all temporal filtering has been performed with a simple Lanczos filter. A Boxcar filter has also been tested, but it did not qualitatively alter the conclusion drawn from the presented results. After filtering with a 5-yr cutoff period, the first and last 3 years of the time series have been discarded from further analyses to avoid any boundary effects of the filter.

For validation of the reference simulation (REF), objectively analyzed monthly climatological temperature and salinity data on a $1/4^\circ$ grid, averaged over all six available decades from the *World Ocean Atlas 2013* (WOA13.v2; Locarnini et al. 2013; Zweng et al. 2013) are used. From these temperature and salinity fields, potential density σ_0 is calculated and used to derive geostrophic velocities with a reference depth of 1500 m. Horizontal surface geostrophic velocities derived from sea surface height measurements by satellite altimetry, produced by SSALTO/DUACS and distributed by Archiving, Validation, and Interpretation of Satellite Oceanographic

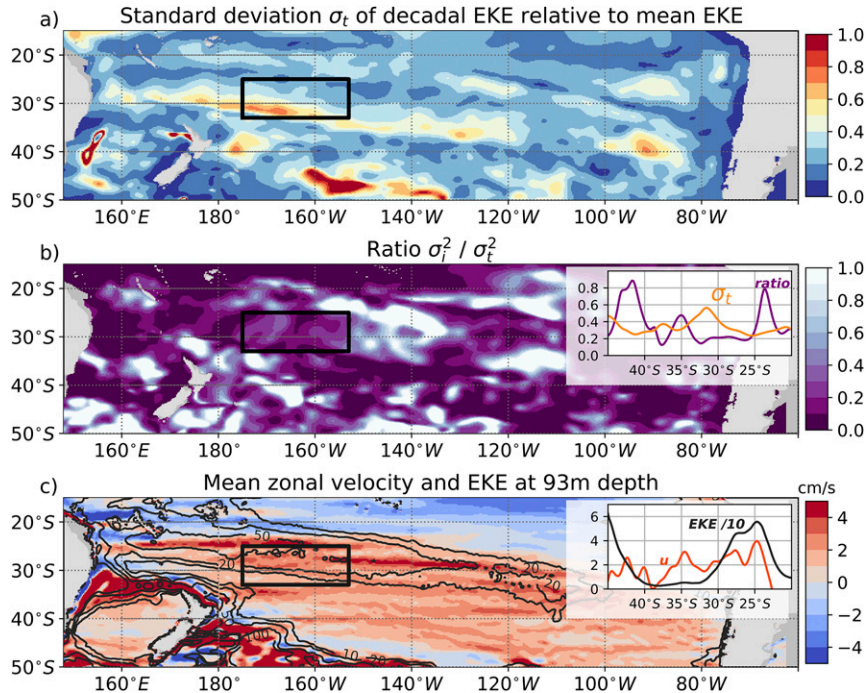


FIG. 2. (a) As in Fig. 1a, but only showing the South Pacific. (b) As in Fig. 1c, but only showing the South Pacific. The small inset shows the zonal averages (averaged over the longitudes of the black box) of the standard deviation depicted in (a) (orange) and the ratio depicted in (b) (purple), both without units. (c) Mean zonal velocity (cm s^{-1}) at 93-m depth from REF. The zonal velocity is positive eastward. Overlying contours show EKE at 93 m from REF. Contour levels are 10, 20, 50, and $100 \text{ cm}^2 \text{ s}^{-2}$. The small inset depicts the zonal averages (averaged over the black box) of zonal velocity u (red; cm s^{-1}) and EKE (black; $\text{cm}^2 \text{ s}^{-2}$ divided by 10). In (a)–(c), the black box indicates the region in which further investigations are conducted.

data (AVISO; <http://www.aviso.altimetry.fr/duacs>) are used to calculate observational surface EKE.

3. Results

a. Intrinsic and forced variability

A large part of the variability in the oceanic meso-scale, even on decadal time scales, is of an intrinsic nature and, therefore, cannot be related to changes in the forcing of the ocean (e.g., O’Kane et al. 2013; also see section 1). Thus, in order to detect significant, deterministic decadal changes of EKE and to attribute an atmospheric driver, the amplitude of these changes should be sufficiently large. Simultaneously, the intrinsic variability in the region should be relatively low, so as to minimize the possibility that the decadal changes in EKE are of an intrinsic nature. The intrinsic variability on decadal time scales is investigated by means of the ratio of intrinsic variance σ_i^2 to total variance σ_t^2 of EKE on decadal time scales (Figs. 1c, 2b).

Following Penduff et al. (2011), σ_i^2 is the variance of low-pass-filtered annual mean EKE, filtered with a 5-yr cutoff period, of the climatological run CLIM, where

the atmosphere does not exhibit any variability on interannual-to-decadal scales. Thus, all decadal variability observed in CLIM’s ocean must arise from processes internal to the ocean. Accordingly, σ_t^2 is the same variance of decadal EKE, but from the simulation with interannual forcing variability (REF). If σ_i^2/σ_t^2 approaches one, most of the variability is generated internally. It should be noted that σ_i^2/σ_t^2 is only an estimate, as the intrinsic variability in REF can be different from the intrinsic variability in CLIM. It has been shown that interannual-to-decadal atmospheric variability is able to trigger modes of internal variability in the ocean (e.g., Taguchi et al. 2010; O’Kane et al. 2013), which are not accounted for in σ_i^2/σ_t^2 .

Over most of the global ocean in REF, the standard deviation of EKE at 93-m depth on decadal time scales σ_t is about 10%–40% of the mean EKE (Fig. 1). Outside the tropics, this is less than the part of variability that can be attributed to processes internal to the ocean. Poleward of 15°N and 15°S, the ratio of intrinsic to total variability σ_i^2/σ_t^2 is above 30%, on average (Fig. 1). Aside from western boundary currents and other strong current systems, the subtropical South Pacific is the only

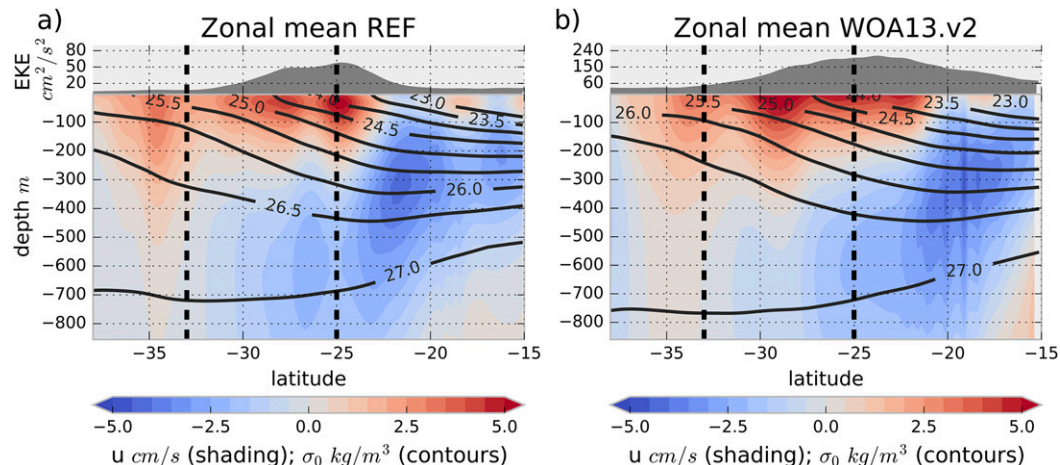


FIG. 3. (a) Zonal mean velocity u (cm s^{-1}) from REF, averaged from 1963 to 2006, against depth (shading). Positive values indicate eastward velocities. Overlying contours show density σ_0 with contours every 0.5 kg m^{-3} from 23.0 to 27.0 kg m^{-3} . In the upper section, zonal mean EKE ($\text{cm}^2 \text{ s}^{-2}$) at 93-m depth is shown. All quantities shown are averaged over the longitudes of the black box shown in Fig. 2. (b) As in (a), but for WOA13.v2 (u , σ_0) and AVISO (EKE) data. In (b), u are geostrophic velocities calculated with a reference depth of 1500 m.

location in the world's oceans where decadal variability with magnitude $>50\%$ of the mean is found along with a relatively low ratio σ_i^2/σ_t^2 (Figs. 1a,c and 2a,b).

We focus further analyses on a box between $25^\circ\text{--}33^\circ\text{S}$ and $175^\circ\text{--}153^\circ\text{W}$. The box is characterized by a large decadal variability of EKE, with σ_t between 30% and more than 70% of the mean EKE, with a zonal mean maximum of 60% at 31°S (Fig. 2a). At the same time, the ratio σ_i/σ_t of intrinsic to total variance of decadal EKE is low. Parameter σ_i/σ_t exhibits a local minimum from <0.1 to 0.3, with a zonal average of 0.2 (Fig. 2b). This combination of large decadal variability and a low ratio of intrinsic to total variability of EKE cannot be found to such an extent in any other subtropical ocean (Figs. 1a,c).

After establishing the exceptional properties of decadal EKE variability in the STCC region, we now describe the mean state of the STCC region in detail and validate the model simulations against observations (sections 3b and 3c), and then we investigate the decadal variability of the EKE associated with the STCC (section 3d) and the associated atmospheric forcing (section 3e).

b. The Subtropical Countercurrent: Mean state

The near-surface circulation from REF in the subtropical South Pacific is dominated by the anticlockwise subtropical gyre with broad eastward flow between roughly 30° and 45°S , and westward flow in the SEC between 15° and 30°S (Fig. 2c). Between 25° and 35°S , slanting southward toward the east; however, bands of eastward velocity are located above the SEC (Fig. 3a).

These eastward velocities have a maximum of $>5 \text{ cm s}^{-1}$ at 25°S and extend down to about 250 m between 25° and 33°S . The SEC below has a maximum of 2.5 cm s^{-1} at 26°S and 600-m depth; the core of the SEC (5 cm s^{-1}), however, lies to the north between 21° and 22°S at 300–400-m depth. While the core of the SEC and the northern edge of the STCC are located 2° to 3° farther north in the geostrophic velocities derived from WOA13.v2 data, the overall structure of the current system compares well between the simulation and the observations (Fig. 3b). Larger differences can only be found in the southern branch of the STCC at 27° to 29°S : that is, roughly 2 cm s^{-1} weaker in REF. The westward flow at depth is stronger in REF, compared to WOA13.v2 inside the box, so that the vertical shear of horizontal velocities remains similar. One cause for this discrepancy could be the choice of the reference depth of 1500 m for the calculation of the geostrophic velocities.

The cause for the reversal of the horizontal flow with depth can be seen in the isopycnals shown in Figs. 3a and 3b. The meridional density gradient at depth is positive to the north, associated with the westward SEC. At 600-m depth, however, the gradient reverses, and in accordance with the thermal wind balance, the westward current weakens toward the surface, reversing at around 250 m. The induced vertical shear in horizontal velocity has been shown to be baroclinically unstable (Qiu and Chen 2004), resulting in a maximum of EKE at the latitude of the largest shear (25°S ; Fig. 3a). The surface EKE from AVISO has a similar meridional distribution between 25° and 33°S ; however, the magnitude of the EKE is roughly 3 times higher in AVISO than in REF

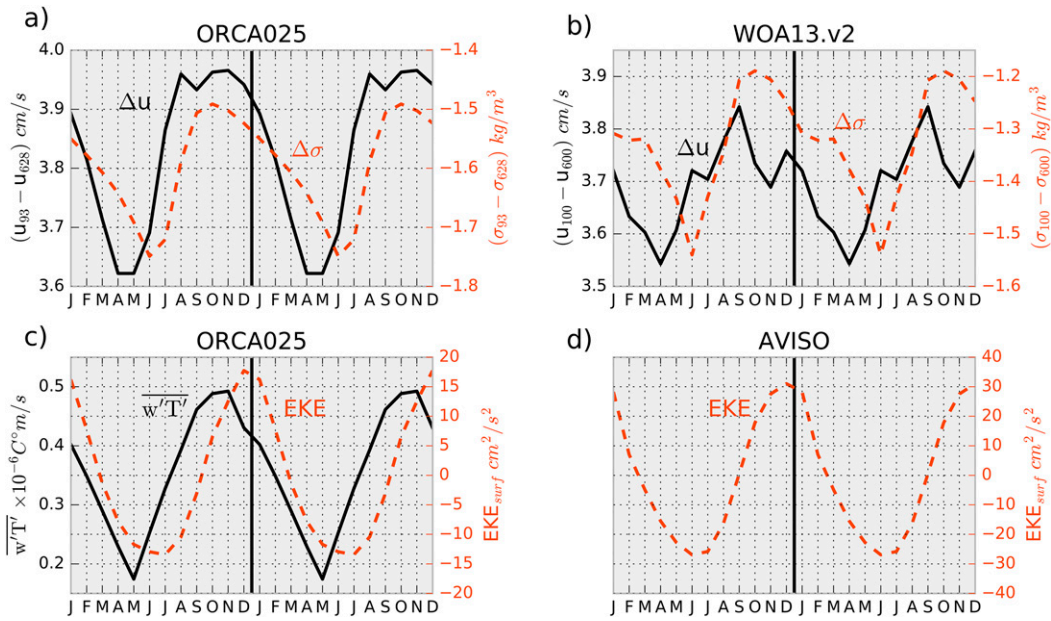


FIG. 4. Climatological seasonal cycles averaged over 25° – 33° S, 153° – 175° W, of (a) simulated (REF) zonal velocity difference Δu (cm s^{-1}) between 93 and 628 m (solid black) and simulated (REF) density difference $\Delta\sigma_0$ (kg m^{-3}) between 93 and 628 m (dashed red). (b) Geostrophic zonal velocity difference Δu (cm s^{-1}) between 100 and 600 m (solid black) and density difference $\Delta\sigma_0$ (kg m^{-3}) between 100 and 600 m (dashed red) based on *WOA13.v2*. (c) Simulated (REF) $\overline{w'T'}$ ($10^{-6} \text{C m s}^{-1}$) averaged from 64 to 322 m (solid black), and simulated (REF) surface EKE ($\text{cm}^2 \text{s}^{-2}$; dashed red). (d) Observed (AVISO) geostrophic surface EKE ($\text{cm}^2 \text{s}^{-2}$). Note the different scales on the y axes of (a), (b) and (c), (d). For an easier interpretation of the results, the seasonal cycles are repeated once on the x axis.

(Fig. 3). Part of this difference can be accounted for by the fact that the EKE from the model is calculated at 93-m depth. Simulated EKE at the surface is twice as large as at 93-m depth, on average, in the STCC region (not accounting for possible ageostrophic contributions). Despite the EKE from satellite altimetry being still 50% higher after accounting for this depth dependency, the $1/4^{\text{th}}$ model is found to be suitable to investigate the temporal variations in EKE in the STCC region, as will be demonstrated in the following section.

c. Seasonal cycle

Changes in stratification and vertical shear of horizontal velocities have been shown to cause decadal variations of baroclinic instability in the STCC region by Travis and Qiu (2017). Using observational data, they showed these variations to manifest themselves in decadal EKE variability. For the extended period from 1960 to 2009 investigated in this study, it is not possible to verify the simulated fields of velocities and stratification against observations because the data coverage from observations is not sufficient. Nevertheless, the simulations can be validated using the seasonal cycle of EKE. The seasonal cycle, similar to the decadal variability, is driven by changes in stratification and shear (Qiu and Chen 2004) that influence baroclinic instability.

To compare REF to observations, monthly climatological values are used. The vertical shear Δu of horizontal velocities in the region 25° – 33° S, 175° – 153° W, is estimated using the difference between zonal velocity at 93 and 628 m (100 and 600 m) in REF (*WOA13.v2*). On average, Δu and the amplitude of its seasonal cycle are 0.1 cm s^{-1} larger in REF, compared to observations (Figs. 4a,b). The phase of the seasonal cycle is similar, though, with a minimum in April (April/May) and largest values in September and December (August and November) in the estimate based on observations (model).

The variations in stratification are estimated using the density difference $\Delta\sigma$ between the same depth levels as for the zonal velocities. Stratification is stronger in REF by 0.3 kg m^{-3} , and the amplitude of the seasonal cycle is slightly larger in the observations (Figs. 4a,b). The phase of the seasonal cycle agrees well between model and observations, with a minimum in June and a maximum in October. Given the seasonal cycles of Δu and $\Delta\sigma$, baroclinic instability should be stronger in austral spring/summer, compared to austral autumn/winter.

We estimate the strength of the baroclinic production mechanisms in the model by calculating $\overline{w'T'}$ as a measure of the energy transfer from the reservoir of eddy available potential energy to EKE (Zhai and Marshall 2013) with w being the vertical velocity and T the potential temperature;

$\overline{(\)}$ denotes the mean over all available data for each month and $(\)'$ denotes the 5-day mean deviation from the monthly climatology. For simplicity, potential temperature T is used here as an estimate for density fluctuations ρ' , and the gravitational constant g in the term $(\overline{w'\rho'}g)$ from Zhai and Marshall (2013) is neglected. Indeed, $\overline{w'T'}$ exhibits a clear seasonal cycle with a minimum in May and a maximum in October/November, followed by a minimum and maximum, respectively, in EKE with a lag of 1 to 2 months (Fig. 4c). A lag between $\overline{w'T'}$ and EKE is to be expected because the instabilities require time to grow, depending on their growth rate. The EKE from AVISO has exactly the same phase as that from the model; however, the amplitude of the seasonal cycle is $\sim 50\%$ larger than in the model (Fig. 4d). This could be partly because of the stronger stratification in the model and partly because the model's resolution is not high enough to simulate the whole spectrum of mesoscale, baroclinic instabilities.

Nevertheless, we have demonstrated that the ORCA025 model is capable of simulating baroclinic instabilities and their seasonal variability in the STCC. This gives confidence in the model's ability to simulate the correct timing of decadal changes of EKE, especially considering their dependence on large-scale properties, such as stratification and vertical shear of horizontal current systems. These decadal changes of EKE will be investigated in the next section.

d. Decadal variability

The EKE in REF inside the box shown in Fig. 2 exhibits large variations on decadal time scales. After an increase in the late 1960s, the 1970s have an average EKE of $40 \text{ cm}^2 \text{ s}^{-2}$ (solid black curve in Fig. 5). EKE decreases again in the mid-1980s, levels off at $20 \text{ cm}^2 \text{ s}^{-2}$, and increases again in the 2000s. To illustrate the atmospherically forced nature of this variability, the variations of EKE from CLIM are shown in Fig. 5 to be less than 50% of REF and to have a completely different phase. Comparing REF to the higher-resolution configuration of the same model ($1/10^\circ$; TROPAC01), mean EKE levels are 1.5 times higher in the higher-resolution run; however, the relative peak to peak amplitude is $\sim 100\%$ of the mean in both simulations, and both simulations show similar phases of EKE variations. Further investigation will be focused on the period 1971–81 and its anomalous, unique properties of the surface ocean.

In section 3b, we demonstrated the importance of meridional density gradients to the STCC-SEC system and thus expect changes in these density gradients to influence the STCC and its EKE. Indeed, corresponding to the elevated EKE in the 1970s, there is a dipole of density anomalies in the subsurface ocean (note that all

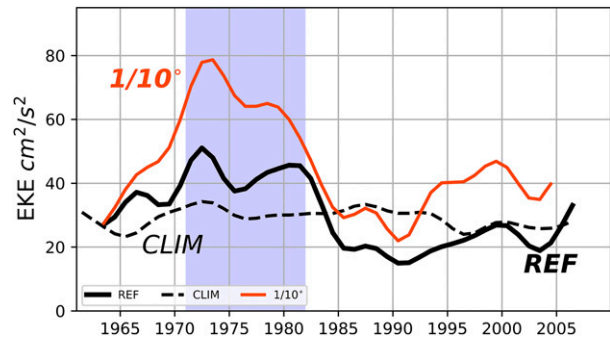


FIG. 5. Time series of EKE ($\text{cm}^2 \text{ s}^{-2}$) at 93-m depth averaged over the black box shown in Fig. 2 ($25^\circ\text{--}33^\circ\text{S}$, $153^\circ\text{--}175^\circ\text{W}$) for REF (solid black), CLIM (dashed black), and a $1/10^\circ$ model (TROPAC01; solid red). All time series in the main plot have been filtered with a 5-yr cutoff period. Blue-shaded area shows the anomalous period from 1971 to 1981.

anomalies are referenced to the period 1960–2009). A positive density anomaly with a maximum of 0.1 kg m^{-3} is centered at 33°S and 300-m depth, collocated with a negative temperature anomaly of up to -0.6°C (Fig. 6a). Farther to the north, at 25°S and 150-m depth, the density is about 0.1 kg m^{-3} lower, compared to the mean. This negative anomaly is supported partly by a positive temperature anomaly of 0.3°C centered at 26°S and 250-m depth. Closer to the surface, at the northern boundary of the box, salinity also plays a role in determining the strength and structure of this density anomaly (Fig. 7).

This anomalous dipole structure steepens the slope of the isopycnals and thus increases the meridional density gradient, especially between 200- and 300-m depth (Fig. 6b). This results in surface-intensified eastward current anomalies of up to 2 cm s^{-1} at the latitudes of the strongest increase in the density gradient (27° and 31°S) arising from the increased vertical shear, resulting in a baroclinically more unstable current system, as already illustrated by Qiu and Chen (2004) for seasonal time scales and Travis and Qiu (2017) for decadal time scales. Figure 8 illustrates the decadal variations of the vertical shear Δu and $\overline{w'T'}$ as an indicator for the baroclinic instability. During 1971–81, Δu exhibits a 20%–30% increase with respect to the mean, and accordingly, $\overline{w'T'}$ is 40%–50% larger. This additional baroclinic instability, in turn, leads to intensified mesoscale variability and elevated EKE in the upper ocean.

e. The role of wind and the interdecadal Pacific oscillation

To determine whether the subsurface temperature anomalies are caused by variations in buoyancy or momentum fluxes at the atmosphere–ocean interface, the two model runs BUOY and WIND are used. It can be

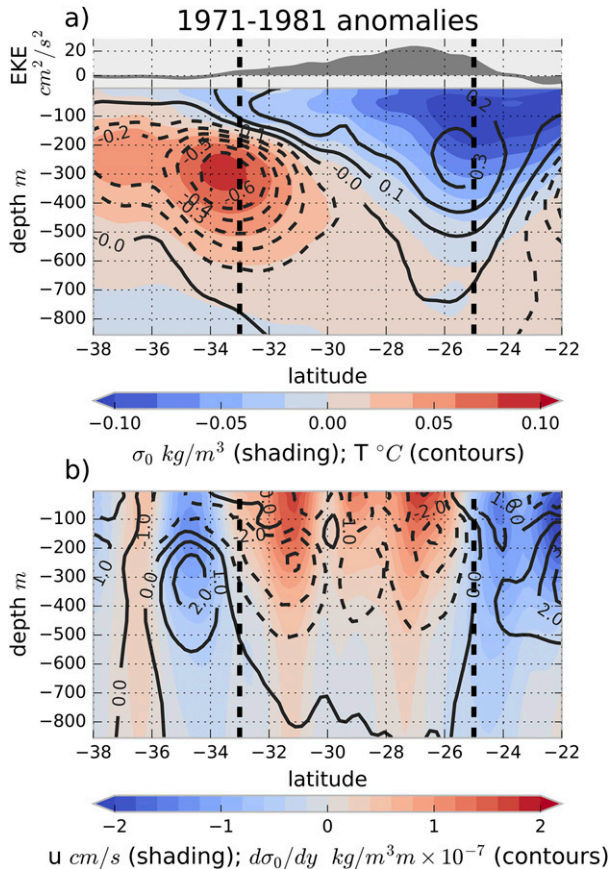


FIG. 6. (a) The 1971–81 anomaly of zonal mean density σ_0 (REF) against depth (shading). Overlying contours show temperature anomalies with contours every 0.1°C from -0.6° to 0.3°C . In the upper section, the zonal mean EKE anomaly at 93-m depth is shown. (b) The 1971–81 anomaly of zonal velocity u (cm s^{-1}) against depth (shading). Overlying contours show the anomalous zonal mean meridional density gradient $d\sigma_0/dy$. Negative values indicate an increased southward density gradient. Contours are shown every $1 \times 10^{-7} \text{ kg m}^{-3} \text{ m}^{-1}$ from $-3 \times 10^{-7} \text{ kg m}^{-3} \text{ m}^{-1}$. All quantities shown are averaged over the longitudes of the black box shown in Fig. 2 (153° – 175°W). Anomalies are calculated with respect to the 1960–2009 mean.

clearly seen in Fig. 9 that BUOY exhibits only minor decadal variability, while WIND is able to reproduce the decadal variability of EKE found in REF. BUOY shows a minimum of around 25 – $30 \text{ cm}^2 \text{ s}^{-2}$ in the 1970s, when WIND and REF have EKE of approximately 40 – $50 \text{ cm}^2 \text{ s}^{-2}$, followed by a slow increase toward 30 – $40 \text{ cm}^2 \text{ s}^{-2}$ in BUOY, when WIND and REF show a minimum of 15 – $25 \text{ cm}^2 \text{ s}^{-2}$ in the 1980s and 1990s. The decadal variability in BUOY is of the same order of magnitude as in CLIM and could thus be of intrinsic nature. After establishing the essential role of the wind forcing for variations of the STCC and EKE, the responsible mechanisms will now be explored.

From Fig. 10, it can be seen that the density anomalies at depth (322 m, the depth at which the anomalies are strongest) are related to wind stress curl anomalies at the surface to a certain extent. The positive wind stress curl anomaly in the early 1970s triggers anomalous downwelling between 26° and 38°S . This leads to density anomalies at depth, with the maximum in the thermocline, where the vertical temperature gradient is strongest. Anomalies in salinity can also be observed, though they are not dominant in determining the density structure (cf. Fig. 7).

In the late 1970s, a negative anomaly in wind stress curl then induces upwelling from $\sim 28^{\circ}\text{S}$ toward the south. The maximum negative temperature anomaly is located slightly deeper than the positive anomaly farther north (Fig. 6), as the strongest vertical gradient in temperature, the thermocline, is located deeper at these latitudes. As there are no associated anomalies on density surfaces (not shown), both these temperature anomalies are of an adiabatic nature, as expected for anomalies associated to wind-driven upwelling and downwelling.

Interestingly, the positive subsurface density anomaly in the early 1970s and the negative density anomaly in the late 1970s are both shifted northward with respect to the related wind stress curl anomalies by roughly 3° latitude (Fig. 10), rather than being located directly beneath the wind stress curl anomalies, where the upwelling and downwelling should occur. The most obvious reason for that 3° shift is the propagation of density anomalies into the region from the east. These anomalies are generated in the eastern South Pacific (25° – 33°S , 110° – 120°W), where local wind stress curl anomalies generate subsurface density anomalies (Fig. 11). In contrast to the wind stress curl anomalies in the western part of the basin, these anomalies occur on time scales shorter than 5 years. To focus on the influence of these interannual anomalies while also excluding shorter, more synoptic variability, the density anomalies in Fig. 11 have been bandpass filtered to include only variability on time scales of 2–5 years. The density anomalies propagate westward at a speed of $\sim 6 \text{ cm s}^{-1}$, arriving in the box investigated (153° – 175°W) after roughly 2–3 years. This propagation speed lies within the observed range of Rossby wave propagation speed at these latitudes from satellite altimetry (e.g., Chelton and Schlax 1996).

Subdecadal density anomalies at 153° – 164° and 164° – 175°W are correlated to the wind stress curl forcing in the eastern part (110° – 120°W) with a lag of 28 and 40 months, respectively (correlation coefficients -0.38 and -0.30 , both significant at the 95% level). More precisely, a negative density anomaly of up to

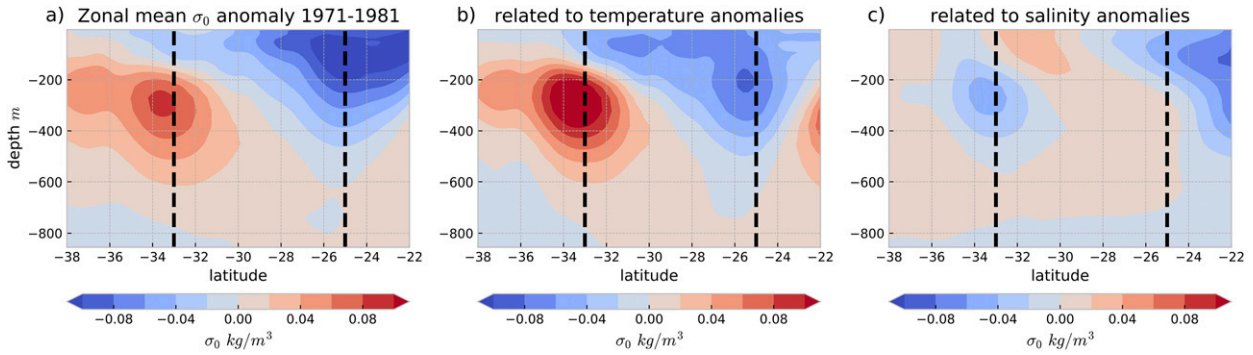


FIG. 7. (a) The 1971–81 anomaly of zonal mean density σ_0 (REF) against depth (shading). (b) Density σ_0 calculated from mean salinity and anomalous temperature to illustrate the effect of temperature anomalies on the density distribution. (c) Density σ_0 calculated from mean temperature and anomalous salinity to illustrate the effect of salinity anomalies on the density distribution. All quantities shown are averaged over the longitudes of the black box shown in Fig. 2 (153° – 175° W). The latitudes of the box are indicated by the vertical, dashed black lines. Anomalies are calculated with respect to the 1960–2009 mean.

-0.03 kg m^{-3} arrives in the box in the early 1970s, supporting the negative anomaly generated by the local wind stress curl forcing. In 1975, a strong positive anomaly of 0.03 kg m^{-3} is arriving at the same time the local wind stress curl forcing switches from positive to negative. Comparing the magnitudes in Figs. 10 and 11, it is obvious that in the 1970s, between 30% and 40% of the local density anomalies can be explained by signals arriving in the western basin that originate from farther east.

In the 1980s and early 1990s, both the local (in the western part) and eastern wind stress curl anomalies are weak (associated density changes are $<0.03 \text{ kg m}^{-3}$) and do not induce any significant changes in current strength and EKE (Fig. 9). The late 1990s and 2000s exhibit a weak increase in EKE, which is associated with strengthened local and remote (eastern) wind stress curl anomalies. However, the local wind stress curl anomalies exhibit a second maximum at $\sim 35^\circ$ S in contrast to the 1970s, when a minimum occurred at this latitude (Fig. 10). In combination with a negative density anomaly arriving from the east around the year 2000 (Fig. 11), this results in meridionally almost-uniform subsurface density anomalies that do not change the meridional gradient significantly.

The decadal variability of the large-scale wind field over the South Pacific can, to a large degree, be understood in terms of the IPO. The wind stress curl at 33° S between 153° and 175° W is correlated to the IPO index, with a correlation coefficient of -0.34 at time scales >5 years (also cf. Figs. 10a,b). To investigate the role of the IPO in forcing the simulated changes in the STCC, the simulation IPOsim as described in section 2 is used. In Fig. 9, the green line shows the temporal evolution of EKE in the box in IPOsim to be quite similar to the REF and WIND cases. There is a strong increase in EKE in the early 1970s and a slow decrease afterward,

until the end of the IPOsim simulation. However, the second peak in EKE in the late 1970s is not captured in the IPOsim run. This is due to a weaker negative wind stress curl anomaly at the southern edge of the box in IPOsim; thus, the meridional density gradient is not reinforced. This might be caused by the transition time between the negative and positive IPO phases. The IPOsim simulation uses wind fields from completely negative and positive IPO phases and does not fully account for the transition between these. In reality, the transition might be much more complex than the linearly interpolated attempt presented here, thus possibly explaining the differences between WIND and IPO.

The question arises why EKE does not increase in a similar fashion in the 2000s, when the IPO again is in a negative phase. In addition to the meridional structure of the density anomaly in the 2000s, which is different from the 1970s due to a different structure of the local wind stress curl anomaly, and also the effect of density anomalies arriving from the east (Figs. 10, 11), a second

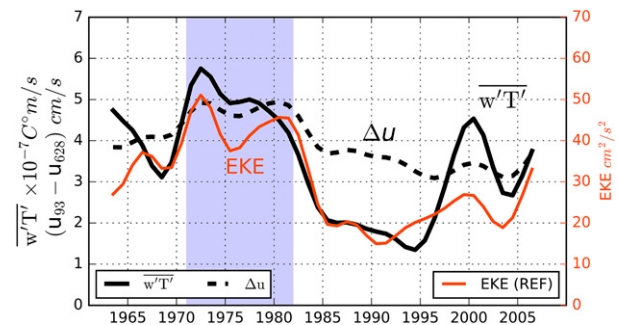


FIG. 8. Time series averaged over 25° – 33° S, 153° – 175° W, of simulated (REF) $\overline{w'T'}$ ($10^{-7} \text{ }^\circ\text{C m s}^{-1}$) averaged from 64 to 322 m (solid black), simulated (REF) zonal velocity difference Δu between 93- and 628-m depth (cm s^{-1} ; dashed black), and simulated (REF) EKE ($\text{cm}^2 \text{ s}^{-2}$) at 93-m depth (solid red).

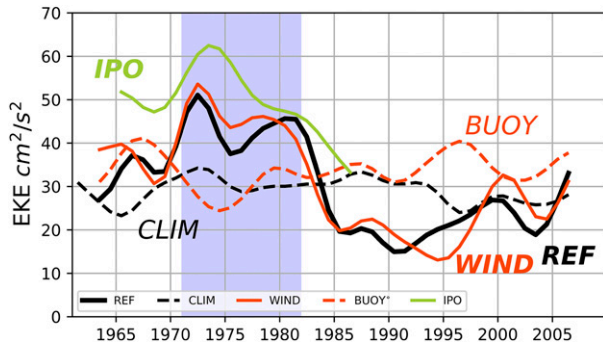


FIG. 9. Time series of EKE at 93-m depth averaged over the black box shown in Fig. 2 (25°–33°S, 153°–175°W) for REF (solid black), CLIM (dashed black), WIND (solid red), BUOY (dashed red), and IPOsim (green). Blue-shaded area shows the period over which anomalies are averaged.

explanation can be brought forward. While the magnitude of the negative IPO phase in the 2000s is about as large as in the 1970s, the duration is much shorter. In the early decades, the IPO is in a mostly negative phase in the 1960s; the index then slowly decreases until 1975 and then abruptly increases, reaching positive values in 1977. This results in more than 10 years of negative IPO forcing. Around the year 2000, the IPO index becomes

negative in 1998, reaches its minimum in 2000, and shows positive values already in 2002, resulting in only 4 years of negative IPO forcing. Thus, the response of EKE is much weaker, though nonetheless present, around 2000, with a short peak in the late 1990s and early 2000s.

In summary, the IPO seems to set the large-scale background wind field that either favors or suppresses the increase of STCC strength through the induced anomalies of the meridional density gradient. However, additional factors are needed to ultimately set the strength of the STCC and EKE levels. In the 1970s, wind stress curl anomalies in the eastern basin aid with the generation of density anomalies that propagate to the west and make up 30%–40% of the observed anomalies in the western basin. These eastern wind stress curl anomalies are not associated with the IPO (correlation coefficient between the IPO index and wind stress curl averaged over 25°–33°S, 110°–120°W, is 0.02).

4. Summary and conclusions

Using an eddy-permitting global ocean general circulation model, we investigate a band of decadal variability of near-surface EKE in the subtropical South Pacific (25°–33°S, 175°–153°W). This region exhibits a

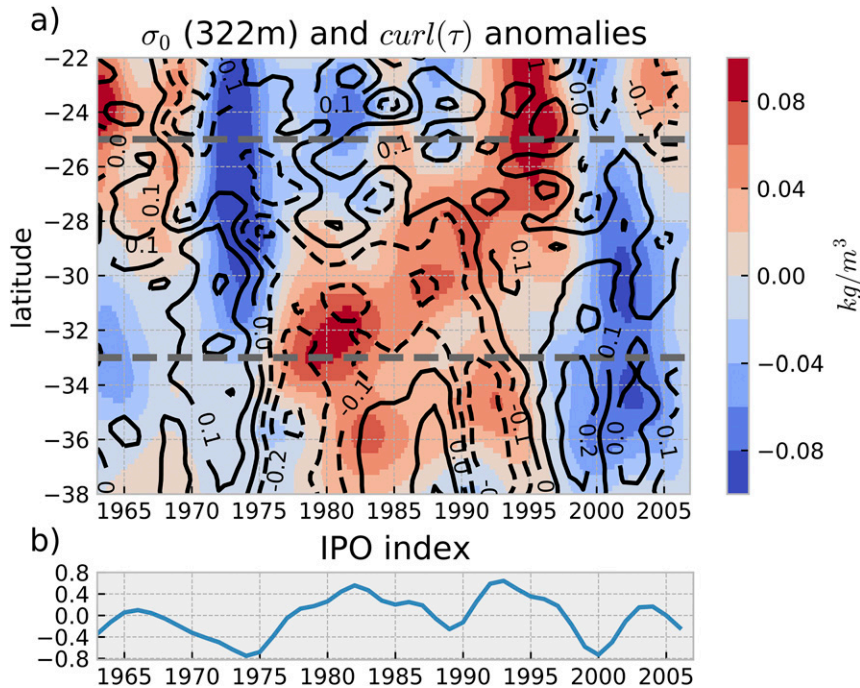


FIG. 10. (a) Zonal mean density σ_0 anomalies at 322-m depth (averaged over the longitudes of the black box shown in Fig. 2; the latitudinal extent is indicated here by the dashed gray lines) over time (shading). Overlying contours depict wind stress curl anomalies. Contours are drawn every $0.1 \times 10^7 \text{ N m}^{-2}$ from -0.3 to $0.3 \times 10^7 \text{ N m}^{-2}$. Anomalies are calculated with respect to the 1960–2009 mean, detrended, and filtered with a 5-yr cutoff period Lanczos filter. (b) IPO index (from Henley et al. 2015) filtered with a 5-yr cutoff period Lanczos filter.

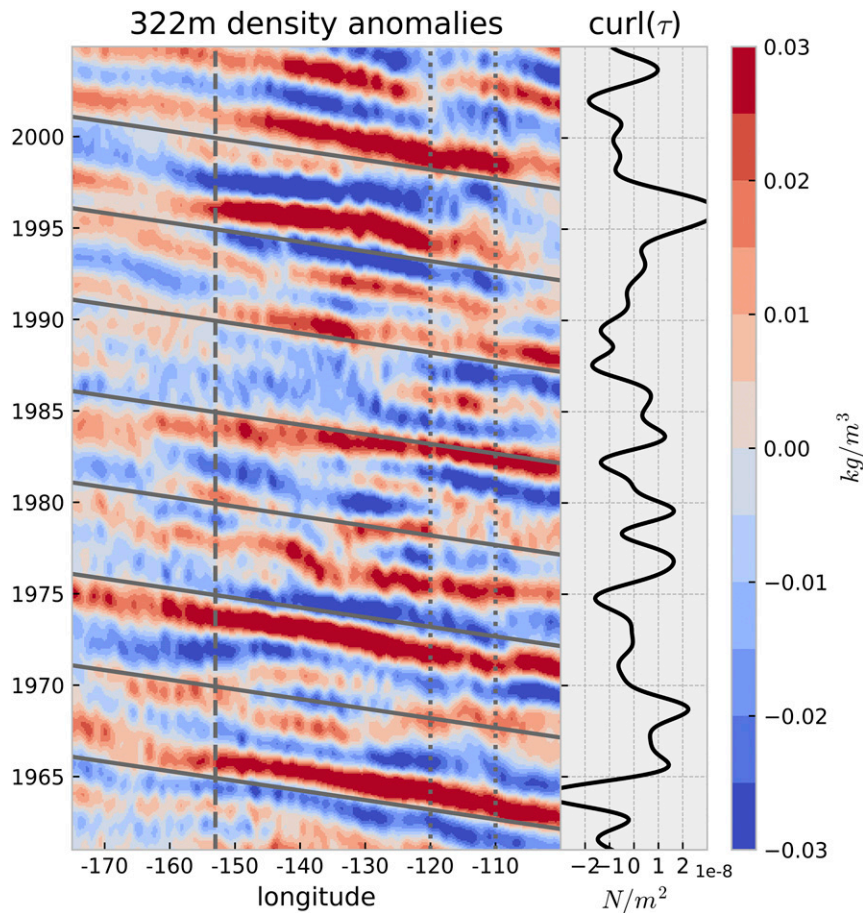


FIG. 11. Meridional mean density σ_0 anomalies (averaged over the latitudes of the black box shown in Fig. 2, whose longitudinal extent is indicated by the dashed gray line) at 322-m depth over time. Gray solid lines represent the theoretical path of an anomaly propagating westward with speed of 6 cm s^{-1} , which is in the range of observed speeds for Rossby waves at these latitudes (Chelton and Schlax 1996). The solid black line in the right panel depicts the wind stress curl anomaly averaged over $25^\circ\text{--}33^\circ\text{S}$, $110^\circ\text{--}120^\circ\text{W}$ (indicated by the two vertical, dotted gray lines). Density and wind stress curl are bandpass filtered, only retaining periods of 2–5 years. Anomalies are calculated with respect to the 1960–2009 mean.

unique feature among the subtropical gyres of the world's oceans: significant, atmospherically forced, decadal EKE variability. Over most of the other subtropical oceans, decadal variations of EKE are small and masked by processes internal to the ocean.

The investigated region contains a vertically sheared current system, consisting of the eastward Subtropical Countercurrent in the upper 300 m and the westward South Equatorial Current below. As shown by previous studies based on observations (Qiu and Chen 2004), and confirmed in this study, this vertical shear in horizontal velocities is maintained by the meridional density gradient across the STCC, and the current system is baroclinically unstable, resulting in a local maximum of near-surface EKE. The $1/4^\circ$ OGCM is able to reproduce

the salient features of the seasonal cycles of EKE, baroclinic instability, and its two causes: vertical shear and stratification.

Based on the fact that decadal variations in EKE are driven by changes in vertical shear and stratification (Travis and Qiu 2017), we investigated the decadal variability of EKE. In the STCC region ($25^\circ\text{--}33^\circ\text{S}$, $175^\circ\text{--}153^\circ\text{W}$) EKE shows decadal variations of over 100% of the mean, with a maximum in the 1970s, which is unmatched in the rest of the simulated period. The phase and amplitude of this decadal variability are supported by findings from a $1/10^\circ$ resolution configuration of the same model, as well as by other model studies. For example, Sasaki et al. (2008) show similar variability of EKE in a region nearby in their $1/10^\circ$ OGCM.

As the meridional density gradient sets the strength of the STCC and its mesoscale variability, anomalies in this density gradient are the cause for changes in near-surface EKE. In the 1970s, a dipole of a negative density anomaly in the STCC region and a positive anomaly just to the south increases the meridional density gradient. These anomalies are focused at thermocline depth, where the vertical density gradient is strongest, and are dominated by temperature changes, which, through the thermal wind balance, result in stronger vertical shear and associated baroclinic production of the STCC-SEC system.

Utilizing sensitivity experiments, we show interannual and decadal variability of the wind field to be the essential driver of changes in the STCC, while changes in air–sea heat and freshwater fluxes are negligible contributors. Positive (negative) anomalies in the large-scale wind stress curl over the STCC drive downwelling (upwelling) in the 1970s that results in anomalies in the subsurface density field and its meridional gradient. While most of the decadal variations of the wind stress curl are related to the IPO (supported by another sensitivity experiment), other local and remote wind stress curl variability significantly influences the density field in the STCC region. Thirty to forty percent of the density anomalies in the 1970s can be explained by interannual variability, propagating into the region from the east and modulating the decadal signal of the IPO.

These interannual density anomalies are correlated to the wind stress curl at 110°–120°W at the same latitude and show no relation to the IPO. They propagate at a speed of $\sim 6 \text{ cm s}^{-1}$, identifying them as long baroclinic Rossby waves (cf. Chelton and Schlax 1996). Travis and Qiu (2017) also find Rossby waves to propagate into the STCC region, explaining part of the SSH variability observed, even though Qiu and Chen (2006) predicted the Rossby waves dynamics to break down in this particular region.

In the 1980s and early 1990s, a positive phase of the IPO prevails and causes an extended period of very low EKE levels. In the late 1990s and into the 2000s, differences in the structure and strength of the local wind stress curl anomalies and the westward-propagating density anomalies suppress a response of the STCC to the negative phase of the IPO. Additionally, the later, negative IPO phase is much shorter than the earlier phase, not allowing for a full adjustment of the ocean. Accordingly, there are only minor similarities between the early (1970s) and late (1990s/2000s) negative phases of the IPO.

The STCC region uniquely demonstrates how large-scale interannual and decadal atmospheric variability can manifest itself in variations of the oceanic mesoscale. At the same time, this study shows a complex interplay of local and remote, interannual and decadal

changes in the wind field and associated oceanic variations, not always allowing for a direct attribution of a forcing to its consequences. Nevertheless, given the STCC's connection to the IPO, a behavior similar to the 1970s can be expected in the future if the IPO switches into a negative phase for a prolonged period. With more in situ and remote sensing systems in place today, current and future changes in the STCC can also be observed and used to validate the presented modeling efforts. Additionally, improved models and better observational coverage can be used to investigate the implications of the decadal changes of EKE in the STCC. The STCC is located in close proximity to a region of subduction (e.g., Tsubouchi et al. 2007; Li 2012). Thus, changes in currents, mesoscale variability, and thermocline structure could influence the subduction and spreading of water masses and tracers.

Acknowledgments. We are grateful to two anonymous reviewers for their helpful comments on the manuscript. The model system has been developed by the ocean modeling group at GEOMAR in the framework of the DRAKKAR collaboration. The authors thank Lavinia Patara for providing output from the CLIM simulation and Franziska U. Schwarzkopf for providing output from the TROPAC01 configuration. All simulations were performed at the North-German Supercomputing Alliance (HLRN). This study contributes to the Cluster of Excellence “The Future Ocean” funded by the DFG. Support from the German Federal Ministry of Education and Research (BMBF) through MiKlip2, subproject 01LP1517D (ATMOS-MODINI) is gratefully acknowledged by RJG. Data shown in this paper are available at <http://data.geomar.de>.

REFERENCES

- Barnier, B., and Coauthors, 2006: Impact of partial steps and momentum advection schemes in a global ocean circulation model at eddy-permitting resolution. *Ocean Dyn.*, **56**, 543–567, <https://doi.org/10.1007/s10236-006-0082-1>.
- , and Coauthors, 2007: Eddy-permitting ocean circulation hindcasts of the past decades. *CLIVAR Exchanges*, No. 42, International CLIVAR Project Office, Southampton, United Kingdom, 8–10.
- , and Coauthors, 2014: DRAKKAR: Developing high resolution ocean components for European Earth system models. *CLIVAR Exchanges*, No. 65, International CLIVAR Project Office, Southampton, United Kingdom, 18–21.
- Barrier, N., J. Deshayes, A.-M. Tréguier, and C. Cassou, 2015: Heat budget in the North Atlantic subpolar gyre: Impacts of atmospheric weather regimes on the 1995 warming event. *Prog. Oceanogr.*, **130**, 75–90, <https://doi.org/10.1016/j.poccean.2014.10.001>.
- Chelton, D. B., and M. G. Schlax, 1996: Global observations of oceanic Rossby waves. *Science*, **272**, 234–238, <https://doi.org/10.1126/science.272.5259.234>.

- Combes, V., and E. Di Lorenzo, 2007: Intrinsic and forced interannual variability of the Gulf of Alaska mesoscale circulation. *Prog. Oceanogr.*, **75**, 266–286, <https://doi.org/10.1016/j.pocean.2007.08.011>.
- Czeschel, R., L. Stramma, F. U. Schwarzkopf, B. S. Giese, A. Funk, and J. Karstensen, 2011: Middepth circulation of the eastern tropical South Pacific and its link to the oxygen minimum zone. *J. Geophys. Res.*, **116**, C01015, <https://doi.org/10.1029/2010JC006565>.
- Debreu, L., C. Vouland, and E. Blayo, 2008: AGRIF: Adaptive grid refinement in Fortran. *Comput. Geosci.*, **34**, 8–13, <https://doi.org/10.1016/j.cageo.2007.01.009>.
- Feng, M., C. W. Böning, A. Biastoch, E. Behrens, E. Weller, and Y. Masumoto, 2011: The reversal of the multi-decadal trends of the equatorial Pacific easterly winds, and the Indonesian Throughflow and Leeuwin Current transports. *Geophys. Res. Lett.*, **38**, L11604, <https://doi.org/10.1029/2011GL047291>.
- Grégorio, S., T. Penduff, G. Sérazin, J.-M. Molines, B. Barnier, and J. Hirschi, 2015: Intrinsic variability of the Atlantic meridional overturning circulation at interannual-to-multidecadal time scales. *J. Phys. Oceanogr.*, **45**, 1929–1946, <https://doi.org/10.1175/JPO-D-14-0163.1>.
- Griffies, S. M., and Coauthors, 2009: Coordinated Ocean-Ice Reference Experiments (COREs). *Ocean Modell.*, **26**, 1–46, <https://doi.org/10.1016/j.ocemod.2008.08.007>.
- Henley, B. J., J. Gergis, D. J. Karoly, S. Power, J. Kennedy, and C. K. Folland, 2015: A tripole index for the interdecadal Pacific oscillation. *Climate Dyn.*, **45**, 3077–3090, <https://doi.org/10.1007/s00382-015-2525-1>.
- Jia, F., L. Wu, J. Lan, and B. Qiu, 2011a: Interannual modulation of eddy kinetic energy in the southeast Indian Ocean by southern annular mode. *J. Geophys. Res.*, **116**, C02029, <https://doi.org/10.1029/2010JC006699>.
- , —, and B. Qiu, 2011b: Seasonal modulation of eddy kinetic energy and its formation mechanism in the southeast Indian Ocean. *J. Phys. Oceanogr.*, **41**, 657–665, <https://doi.org/10.1175/2010JPO4436.1>.
- Kobashi, F., and A. Kubokawa, 2012: Review on North Pacific Subtropical Countercurrents and subtropical fronts: Role of mode waters in ocean circulation and climate. *J. Oceanogr.*, **68**, 21–43, <https://doi.org/10.1007/s10872-011-0083-7>.
- Large, W. G., and S. G. Yeager, 2009: The global climatology of an interannually varying air–sea flux data set. *Climate Dyn.*, **33**, 341–364, <https://doi.org/10.1007/s00382-008-0441-3>.
- Li, Z., 2012: Interannual and decadal variability of the subtropical mode water formation in the South Pacific Ocean. *Ocean Modell.*, **47**, 96–112, <https://doi.org/10.1016/j.ocemod.2012.02.001>.
- Locarnini, R. A., and Coauthors, 2013: *Temperature*. Vol. 1, *World Ocean Atlas 2013*, NOAA Atlas NESDIS 73, 40 pp.
- Lorbacher, K., J. Dengg, C. W. Böning, and A. Biastoch, 2010: Regional patterns of sea level change related to interannual variability and multidecadal trends in the Atlantic meridional overturning circulation. *J. Climate*, **23**, 4243–4254, <https://doi.org/10.1175/2010JCLI3341.1>.
- Lübbecke, J. F., C. W. Böning, and A. Biastoch, 2008: Variability in the subtropical-tropical cells and its effect on near-surface temperature of the equatorial Pacific: A model study. *Ocean Sci.*, **4**, 73–88, <https://doi.org/10.5194/os-4-73-2008>.
- Madec, G., P. Delecluse, M. Imbard, and C. Levy, 1998: OPA 8.1 ocean general circulation model reference manual. LODYC–IPSL Tech. Note 11, 91 pp.
- Menezes, V. V., H. E. Phillips, A. Schiller, N. L. Bindoff, C. M. Domingues, and M. L. Vianna, 2014: South Indian Countercurrent and associated fronts. *J. Geophys. Res. Oceans*, **119**, 6763–6791, <https://doi.org/10.1002/2014JC010076>.
- , —, M. L. Vianna, and N. L. Bindoff, 2016: Interannual variability of the South Indian Countercurrent. *J. Geophys. Res. Oceans*, **121**, 3465–3487, <https://doi.org/10.1002/2015JC011417>.
- Merle, J., H. Rotschi, and B. Voituriez, 1969: Zonal circulation in the tropical western South Pacific at 170°E. *Bull. Japan Soc. Fish. Oceanogr., Special Issue (Prof. Uda's Commemorative Papers)*, 91–98.
- Morris, M., D. Roemmich, and B. Cornuelle, 1996: Observations of variability in the South Pacific Subtropical Gyre. *J. Phys. Oceanogr.*, **26**, 2359–2380, [https://doi.org/10.1175/1520-0485\(1996\)026<2359:OOVITS>2.0.CO;2](https://doi.org/10.1175/1520-0485(1996)026<2359:OOVITS>2.0.CO;2).
- O’Kane, T. J., R. J. Matear, M. A. Chamberlain, J. S. Risbey, B. M. Sloyan, and I. Horenko, 2013: Decadal variability in an OGCM Southern Ocean: Intrinsic modes, forced modes and metastable states. *Ocean Modell.*, **69**, 1–21, <https://doi.org/10.1016/j.ocemod.2013.04.009>.
- Penduff, T., B. Barnier, W. K. Dewar, and J. J. O’Brien, 2004: Dynamical response of the oceanic eddy field to the North Atlantic Oscillation: A model–data comparison. *J. Phys. Oceanogr.*, **34**, 2615–2629, <https://doi.org/10.1175/JPO2618.1>.
- , M. Juza, L. Brodeau, G. C. Smith, B. Barnier, J.-M. Molines, A.-M. Treguier, and G. Madec, 2010: Impact of global ocean model resolution on sea-level variability with emphasis on interannual time scales. *Ocean Sci.*, **6**, 269–284, <https://doi.org/10.5194/os-6-269-2010>.
- , —, B. Barnier, J. Zika, W. K. Dewar, A.-M. Treguier, J.-M. Molines, and N. Audiffren, 2011: Sea level expression of intrinsic and forced ocean variabilities at interannual time scales. *J. Climate*, **24**, 5652–5670, <https://doi.org/10.1175/JCLI-D-11-00077.1>.
- Qiu, B., 1999: Seasonal eddy field modulation of the North Pacific Subtropical Countercurrent: TOPEX/Poseidon observations and theory. *J. Phys. Oceanogr.*, **29**, 2471–2486, [https://doi.org/10.1175/1520-0485\(1999\)029<2471:SEFMOT>2.0.CO;2](https://doi.org/10.1175/1520-0485(1999)029<2471:SEFMOT>2.0.CO;2).
- , and S. Chen, 2004: Seasonal modulations in the eddy field of the South Pacific Ocean. *J. Phys. Oceanogr.*, **34**, 1515–1527, [https://doi.org/10.1175/1520-0485\(2004\)034<1515:SMITEF>2.0.CO;2](https://doi.org/10.1175/1520-0485(2004)034<1515:SMITEF>2.0.CO;2).
- , and —, 2006: Decadal variability in the large-scale sea surface height field of the South Pacific Ocean: Observations and causes. *J. Phys. Oceanogr.*, **36**, 1751–1762, <https://doi.org/10.1175/JPO2943.1>.
- , and —, 2010: Interannual variability of the North Pacific Subtropical Countercurrent and its associated mesoscale eddy field. *J. Phys. Oceanogr.*, **40**, 213–225, <https://doi.org/10.1175/2009JPO4285.1>.
- Rieck, J. K., C. W. Böning, R. J. Greatbatch, and M. Scheinert, 2015: Seasonal variability of eddy kinetic energy in a global high-resolution ocean model. *Geophys. Res. Lett.*, **42**, 9379–9386, <https://doi.org/10.1002/2015GL066152>.
- Roemmich, D., J. Gilson, P. Sutton, and N. Zilberman, 2016: Multidecadal change of the South Pacific Gyre circulation. *J. Phys. Oceanogr.*, **46**, 1871–1883, <https://doi.org/10.1175/JPO-D-15-0237.1>.
- Rühs, S., K. Getzlaff, J. V. Durgadoo, A. Biastoch, and C. W. Böning, 2015: On the suitability of North Brazil Current transport estimates for monitoring basin-scale AMOC changes. *Geophys. Res. Lett.*, **42**, 8072–8080, <https://doi.org/10.1002/2015GL065695>.

- Sasaki, Y. N., S. Minobe, N. Schneider, T. Kagimoto, M. Nonaka, and H. Sasaki, 2008: Decadal sea level variability in the South Pacific in a global eddy-resolving ocean model hindcast. *J. Phys. Oceanogr.*, **38**, 1731–1747, <https://doi.org/10.1175/2007JPO3915.1>.
- Schwarzkopf, F. U., 2016: Ventilation pathways in the tropical Atlantic and Pacific Oceans with a focus on the oxygen minimum zones: Development and application of a nested high-resolution global model system. Ph.D. thesis, Christian-Albrechts-Universität zu Kiel, 259 pp.
- Sérazin, G., T. Penduff, S. Grégorio, B. Barnier, J.-M. Molines, and L. Terray, 2015: Intrinsic variability of sea level from global ocean simulations: Spatiotemporal scales. *J. Climate*, **28**, 4279–4292, <https://doi.org/10.1175/JCLI-D-14-00554.1>.
- , B. Meyssignac, T. Penduff, L. Terray, B. Barnier, and J.-M. Molines, 2016: Quantifying uncertainties on regional sea level change induced by multidecadal intrinsic oceanic variability. *Geophys. Res. Lett.*, **43**, 8151–8159, <https://doi.org/10.1002/2016GL069273>.
- , and Coauthors, 2017: A global probabilistic study of the ocean heat content low-frequency variability: Atmospheric forcing versus oceanic chaos. *Geophys. Res. Lett.*, **44**, 5580–5589, <https://doi.org/10.1002/2017GL073026>.
- Steele, M., R. Morley, and W. Ermold, 2001: PHC: A global ocean hydrography with a high quality Arctic Ocean. *J. Climate*, **14**, 2079–2087, [https://doi.org/10.1175/1520-0442\(2001\)014<2079:PAGOHW>2.0.CO;2](https://doi.org/10.1175/1520-0442(2001)014<2079:PAGOHW>2.0.CO;2).
- Taguchi, B., B. Qiu, M. Nonaka, H. Sasaki, S. P. Xie, and N. Schneider, 2010: Decadal variability of the Kuroshio Extension: Mesoscale eddies and recirculations. *Ocean Dyn.*, **60**, 673–691, <https://doi.org/10.1007/s10236-010-0295-1>.
- Travis, S., and B. Qiu, 2017: Decadal variability in the South Pacific Subtropical Countercurrent and regional mesoscale eddy activity. *J. Phys. Oceanogr.*, **47**, 499–512, <https://doi.org/10.1175/JPO-D-16-0217.1>.
- Tsubouchi, T., T. Suga, and K. Hanawa, 2007: Three types of South Pacific Subtropical Mode Waters: Their relation to the large-scale circulation of the South Pacific subtropical gyre and their temporal variability. *J. Phys. Oceanogr.*, **37**, 2478–2490, <https://doi.org/10.1175/JPO3132.1>.
- Ummenhofer, C. C., F. U. Schwarzkopf, G. Meyers, E. Behrens, A. Biastoch, and C. W. Böning, 2013: Pacific Ocean contribution to the asymmetry in eastern Indian Ocean variability. *J. Climate*, **26**, 1152–1171, <https://doi.org/10.1175/JCLI-D-11-00673.1>.
- van Sebille, E., J. Sprintall, F. U. Schwarzkopf, A. S. Gupta, A. Santoso, M. H. England, A. Biastoch, and C. W. Böning, 2014: Pacific-to-Indian Ocean connectivity: Tasman leakage, Indonesian Throughflow, and the role of ENSO. *J. Geophys. Res. Oceans*, **119**, 1365–1382, <https://doi.org/10.1002/2013JC009525>.
- Wilson, C., C. W. Hughes, and J. R. Blundell, 2015: Forced and intrinsic variability in the response to increased wind stress of an idealized Southern Ocean. *J. Geophys. Res. Oceans*, **120**, 113–130, <https://doi.org/10.1002/2014JC010315>.
- Zhai, X., and D. P. Marshall, 2013: Vertical eddy energy fluxes in the North Atlantic subtropical and subpolar gyres. *J. Phys. Oceanogr.*, **43**, 95–103, <https://doi.org/10.1175/JPO-D-12-021.1>.
- Zweng, M., and Coauthors, 2013: *Salinity*. Vol. 2, *World Ocean Atlas 2013*, NOAA Atlas NESDIS 74, 39 pp.